

Analysis and experiments of the dissipative Twistcar: direction reversal and asymptotic approximations

R. Levy¹, A. Dantus¹, Z. Yu¹, and Y. Or^{1*}

Abstract—Underactuated wheeled vehicles are commonly studied as nonholonomic systems with periodic actuation. Twistcar is a classical example inspired by a riding toy, which has been analyzed using a planar model of a dynamical system with nonholonomic constraints. Most of the previous analyses did not account for energy dissipation due to friction. In this work, we study a theoretical two-link model of the Twistcar while incorporating dissipation due to rolling resistance. We obtain asymptotic expressions for the system’s small-amplitude steady-state periodic dynamics, which reveals the possibility of reversing the direction of motion upon varying the geometric and mass properties of the vehicle. Next, we design and construct a robotic prototype of the Twistcar whose center-of-mass position can be shifted by adding and removing a massive block, enabling demonstration of the Twistcar’s direction reversal phenomenon. We also conduct parameter fitting for the frictional resistance in order to improve agreement with experiments.

Index Terms—Robotics, Under-actuated systems, nonholonomic dynamics, asymptotic analysis.

I. INTRODUCTION

UNDERACTUATED locomotive systems are systems whose number of degrees-of-freedom (DoF) is greater than the number of its controlled inputs. Such systems often incorporate nonholonomic constraints [1], [2], which restrict permissible velocity directions without decreasing the effective number of DoF of the system. Examples of such systems can be found in terrestrial motion, such as the Snakeboard [3] and the three-wheeled snake [4], or for swimming in fluid, including Purcell’s swimmer [5], [6] and inertia-dominated swimmers [7]–[9].

Based on the number of constraints and DoF, those systems can be classified as purely kinematic [10] or mixed kinematic-dynamic systems [11]. Purely kinematic systems, such as the three-linked kinematic snake [12] and Purcell’s swimmer, contain an equal number of nonholonomic constraints and passive (unactuated) DoF of body motion. This property leads to body motion that is governed only by the geometric changes of the robot’s actuated inputs of shape variables. When the number of constraints is smaller, changes in the system’s momentum influence its movement alongside the kinematic constraints [13]. A classical example of a mixed system is Chaplygin’s sleigh [14], and its extensions with oscillatory actuation, such as the Chaplygin’s beanie [15] and Chaplygin sleigh with a moving mass [16]. Other examples consist of

wheeled rolling board toys such as the Snakeboard and Roller-racer [17], which is also known in the literature as the Landfish [18], Land-shark [19] or Twistcar [20] - all are renamed variants of the same toy, originally called Roller-racer.

The Twistcar, shown in figure 1, is an underactuated two-linked vehicle with passive wheels. The vehicle is actuated under time-periodic input of the relative angle between the two links. Previous work included a perturbation analysis [21] on a point-mass model [20] and was extended by considering a more general model, incorporating mass and inertia of the two links [22]. It was demonstrated theoretically that a direction reversal in the vehicle’s movement direction is possible by changing the geometric properties of the model. This phenomenon was analyzed in [19], [20], [22] using different approaches. Along with other similar models [23], it has been shown that the non-dissipative nature of the nonholonomic constraints leads to a diverging amplitude of the vehicle’s oscillatory velocity and orientation angle. Importantly, this unbounded behavior does not hold in experiments, as reported in [22], [24].

This theoretically-unbounded behavior arises from the absence of energy dissipation in the system, since the forces maintaining the nonholonomic no-skid constraints do not perform mechanical work. Several methods have been considered to incorporate the wheels’ skid, a behavior also shown in the experiments, into the mathematical model: Some works considered replacing the nonholonomic constraints with a Coulomb’s friction model [22], [25], [26]. Although physically plausible, this hybrid model is numerically sensitive and cannot be studied using analytical tools such as perturbation expansion [20], due to its non-smoothness. The work [19], considered a skid-angle model [27], [28] which mimics skid velocities without adding dissipation to the system. While this model results in smooth dynamics, it still leads to unbounded diverging oscillations due to a lack of dissipation. Another approach introduces dissipation to the system while keeping the nonholonomic no-skid constraints. Recent work [24] suggests using viscous dissipation in rolling resistance of the wheels, and another work used a similar approach on a Snakeboard model [29]. This approach leads to bounded behavior with smooth dynamics.

In this work, we revisit the Twistcar dynamics using the latter assumption of viscous dissipation due to wheels’ rolling resistance, while preserving the nonholonomic no-skid constraints at the lateral directions. We conduct a small-amplitude analysis of the model using perturbation expansion in order to obtain approximate explicit expressions which are compared

This work was supported by Israel Science Foundation under grant no. 1382/23.

¹ Department of Mechanical Engineering, Technion - Israel Institute of Technology, Haifa, Israel

*Corresponding author: izi@technion.ac.il

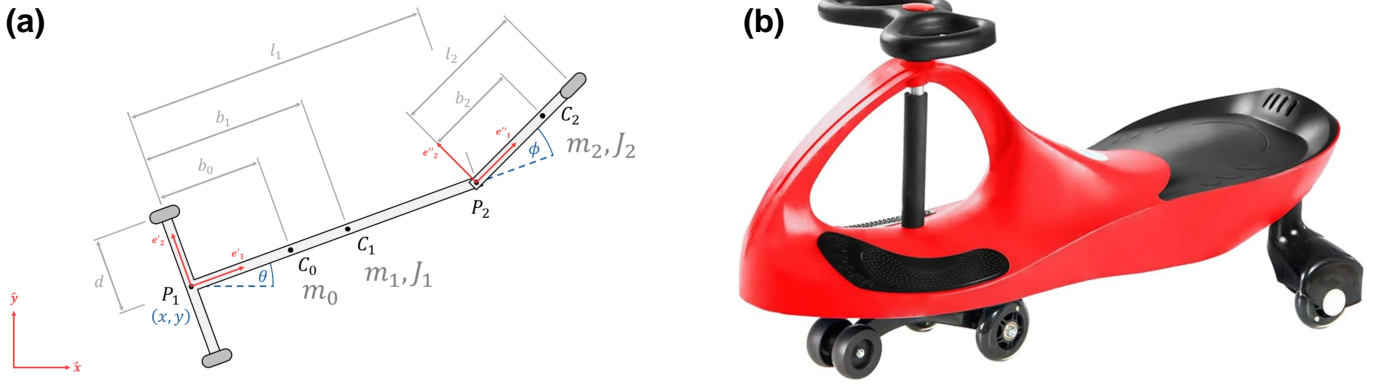


Fig. 1. The Twistcar vehicle. (a) Simplified two-link model. (b) A Twistcar toy example.

to numerical simulations, with excellent agreement for small actuation amplitudes. In addition, we design and construct a robotic prototype of the Twistcar with an open-loop controller of the steering joint's angle. The robot has a modular structure which enables changing the robot's geometry and mass distribution. The perturbation analysis, simulations, and experiments results in a bounded oscillatory motion. Using the asymptotic solution, we obtain explicit conditions for direction reversal due to adding or removing a massive block onto the robot's body. The theoretical predictions are corroborated by the motion of our modular robot, thus demonstrating direction reversal in actual motion experiments.

The paper is organized as follows: In section II we formulate the dynamic equations of the problem, considering the nonholonomic no-skid constraints and the dissipative rolling resistance of the wheels. Then, in section III we conduct numerical simulations demonstrating the bounded behavior of the model and the direction reversal phenomenon. In section IV we obtain approximate asymptotic expressions for the solution of the vehicle's forward speed and orientation angle, assuming small-amplitude actuation. In section V we present the Twistcar robot and experimental results obtained using it. We estimate the viscous dissipation coefficient of the wheels by using parameter fitting between the experimental and numerical results, and demonstrate direction reversal upon shifting the vehicle's center of mass, as predicted by the theoretical analysis. In section VI we discuss additional effects that influence the behavior of the experimental robot - the wheels' skidding and the non-perfectly horizontal terrain on which the experiment was conducted. We show the significance of each effect numerically. Finally, section VII concludes the work and suggests directions for future extensions.

II. PROBLEM FORMULATION

We now present formulation of the Twistcar's dynamic equations of motion, a planar model analogous to that described by [22] as depicted in figure 1. The vehicle has two rigid links, each characterized by a total length l_i , a center of mass (CoM) located at a distance b_i from point P_i , a mass m_i , and a moment of inertia J_i about its CoM. Two wheels are positioned symmetrically at a distance d from point P_1 , while a third wheel is mounted at the apex of link 2. We introduce

a point-mass m_0 , located at a distance b_0 from point P_1 . We choose the following generalized coordinates:

$$\mathbf{q} = [x \quad y \quad \theta \quad \phi]^T \quad (1)$$

Where (x, y) denote the location of point P_1 , θ is the orientation angle of link 1 about the global \hat{x} axis, and ϕ is the relative angle between the links which we refer to as the steering angle. We use the steering angle as the system's input:

$$\phi(t) = \phi_0 + \varepsilon \cos(\omega t) \quad (2)$$

To enforce the no-skid constraints, we express the slip velocities in terms of the generalized coordinates, arrange them in matrix form, and set them to zero. We give the non-holonomic constraints in (3).

$$\mathbf{W}(\mathbf{q})\dot{\mathbf{q}} = \mathbf{0} \quad (3)$$

Where the nonholonomic constraints matrix is:

$$\mathbf{W} = \begin{bmatrix} -\sin \theta & \cos \theta & 0 & 0 \\ -\sin(\theta + \phi) & \cos(\theta + \phi) & l_2 + l_1 \cos \phi & l_2 \end{bmatrix}$$

In order to add viscous rolling resistance to the model, we use Rayleigh's dissipation function, as follows. For each wheel, we define the velocity along its permissible roll direction using the Jacobian:

$$\mathbf{v}_{\parallel, i} = \mathbb{J}_i(\mathbf{q})\dot{\mathbf{q}} \quad (4)$$

Using the Jacobian notation, we define Rayleigh's dissipation function as in (5), where c is the dissipation coefficient.

$$\mathcal{R}(\mathbf{q}, \dot{\mathbf{q}}) = \frac{c}{2} \sum_{i=1}^3 \mathbf{v}_{\parallel, i}^T \mathbf{v}_{\parallel, i} = \frac{c}{2} \dot{\mathbf{q}}^T \left(\sum_{i=1}^3 \mathbb{J}_i(\mathbf{q})^T \mathbb{J}_i(\mathbf{q}) \right) \dot{\mathbf{q}} \quad (5)$$

We differentiate (5) with respect to the generalized velocity $\dot{\mathbf{q}}$ to obtain the dissipation contribution to the dynamic equations. Using the Jacobian notation, one obtains:

$$\mathbf{D}(\mathbf{q}, \dot{\mathbf{q}}) = \frac{\partial \mathcal{R}}{\partial \dot{\mathbf{q}}} = c \left(\sum_{i=1}^3 \mathbb{J}_i(\mathbf{q})^T \mathbb{J}_i(\mathbf{q}) \right) \dot{\mathbf{q}} \quad (6)$$

To derive the constrained dynamic equations of motion, we use the Euler-Lagrange method [30], and include the

nonholonomic forces acting on the model. We use a planar model with constant potential energy to obtain (7).

$$\frac{d}{dt} \left(\frac{\partial T}{\partial \dot{\mathbf{q}}} \right) - \frac{\partial T}{\partial \mathbf{q}} + \frac{\partial \mathcal{R}}{\partial \dot{\mathbf{q}}} = \mathbf{F}_q + \mathbf{W}^T(\mathbf{q})\boldsymbol{\Lambda} \quad (7)$$

Where $\boldsymbol{\Lambda}$ is the vector of forces enforcing the constraints, and \mathbf{F}_q is the vector of generalized forces, which include the actuation torque τ at the steering joint.

$$\boldsymbol{\Lambda} = [\lambda_1 \quad \lambda_2]^T, \quad \mathbf{F}_q = [0 \quad 0 \quad 0 \quad \tau]^T$$

We rearrange (7) in matrix form and differentiate (3) with respect to time. This results in the following differential algebraic system.

$$\begin{aligned} \mathbf{M}(\mathbf{q})\ddot{\mathbf{q}} + \mathbf{B}(\mathbf{q}, \dot{\mathbf{q}}) + \mathbf{D}(\mathbf{q}, \dot{\mathbf{q}}) &= \mathbf{F}_q + \mathbf{W}^T(\mathbf{q})\boldsymbol{\Lambda} \\ \mathbf{W}(\mathbf{q})\dot{\mathbf{q}} + \dot{\mathbf{W}}(\mathbf{q})\dot{\mathbf{q}} &= 0 \end{aligned} \quad (8)$$

Where:

$$\mathbf{M}(\mathbf{q}) = \frac{\partial^2 T}{\partial \dot{\mathbf{q}}^2}, \quad \mathbf{B}(\mathbf{q}, \dot{\mathbf{q}}) = \frac{\partial^2 T}{\partial \dot{\mathbf{q}} \partial \mathbf{q}} \dot{\mathbf{q}} - \frac{\partial T}{\partial \mathbf{q}}$$

III. SIMULATIONS

In this section, we reformulate the dynamic equations in order to conduct numerical analysis. It allows us to obtain time solutions for different model parameters, showing the bounded behavior of the model and the direction reversal phenomenon.

To do so, we divide the generalized coordinates into active coordinates, which we directly control, and passive coordinates.

$$\mathbf{q}_p = [x \quad y \quad \theta]^T, \quad \mathbf{q}_a = \phi \quad (9)$$

We decompose the matrices in (8) with respect to the active and passive coordinates:

$$\begin{aligned} \begin{bmatrix} \mathbf{M}_{pp} & \mathbf{M}_{pa} \\ \mathbf{M}_{pa}^T & \mathbf{M}_{aa} \end{bmatrix} \begin{bmatrix} \ddot{\mathbf{q}}_p \\ \ddot{\mathbf{q}}_a \end{bmatrix} + \begin{bmatrix} \mathbf{B}_p \\ \mathbf{B}_a \end{bmatrix} + \begin{bmatrix} \mathbf{D}_p \\ \mathbf{D}_a \end{bmatrix} &= \begin{bmatrix} \mathbf{0}^{3 \times 1} \\ \tau \end{bmatrix} + \begin{bmatrix} \mathbf{W}_p^T \\ \mathbf{W}_a^T \end{bmatrix} \boldsymbol{\Lambda} \\ \mathbf{W}_p \dot{\mathbf{q}}_p + \mathbf{W}_a \dot{\mathbf{q}}_a + \dot{\mathbf{W}}_p \dot{\mathbf{q}}_p + \dot{\mathbf{W}}_a \dot{\mathbf{q}}_a &= 0 \end{aligned} \quad (10)$$

Where:

$$\begin{aligned} \mathbf{M}_{pp} \in \mathbb{R}^{3 \times 3}, \quad \mathbf{M}_{pa} \in \mathbb{R}^{3 \times 1}, \quad \mathbf{M}_{aa} \in \mathbb{R}, \quad \mathbf{B}_p \in \mathbb{R}^{3 \times 1}, \quad \mathbf{B}_a \in \mathbb{R} \\ \mathbf{D}_p \in \mathbb{R}^{3 \times 1}, \quad \mathbf{D}_a \in \mathbb{R}, \quad \mathbf{W}_p \in \mathbb{R}^{2 \times 3}, \quad \mathbf{W}_a \in \mathbb{R}^{2 \times 1}, \quad \tau \in \mathbb{R} \end{aligned}$$

We rearrange (10) in a new matrix form, where the unknown vector consists of the passive coordinates' acceleration, the actuation torque, and the constraint forces.

$$\begin{bmatrix} \ddot{\mathbf{q}}_p \\ \tau \\ \boldsymbol{\Lambda} \end{bmatrix} = - \begin{bmatrix} \mathbf{M}_{pp} & \mathbf{0}^{3 \times 1} & -\mathbf{W}_p^T \\ \mathbf{M}_{pa}^T & -1 & -\mathbf{W}_a^T \\ \mathbf{W}_p & \mathbf{0}^{2 \times 1} & \mathbf{0}^{2 \times 2} \end{bmatrix}^{-1} \begin{bmatrix} \mathbf{M}_{pa} \ddot{\mathbf{q}}_a + \mathbf{B}_p + \mathbf{D}_p \\ \mathbf{M}_{aa} \ddot{\mathbf{q}}_a + \mathbf{B}_a + \mathbf{D}_a \\ \mathbf{W}_a \ddot{\mathbf{q}}_a + \dot{\mathbf{W}}_p \dot{\mathbf{q}}_p + \dot{\mathbf{W}}_a \dot{\mathbf{q}}_a \end{bmatrix} \quad (11)$$

Using (11), we numerically solve the first three equations to find the time solutions of the passive coordinates $\mathbf{q}_p(t)$. All simulations were conducted using MATLAB's *ode45* function. To obtain the input torque τ and the constraint forces $\boldsymbol{\Lambda}$, we substitute $\mathbf{q}_p(t)$ into the last three equations in (11).

To determine the movement direction and velocity of the vehicle, we examine its velocity along the average direction of progression in world frame. We first simulate under zero initial conditions and obtain the mean value of the steering angle in steady-state $\bar{\theta}$. By substituting $\bar{\theta}$ from the orientation angle's time result, we obtain a solution that oscillates around the world frame's \hat{x} axis.

Simulations were conducted using (11), with an input angle as in (12).

$$\phi_0 = 0, \quad \varepsilon = \frac{\pi}{6}, \quad \omega = 15 [\text{rad/s}] \quad (12)$$

The parameters of the problems were taken under the assumption that each link is a slender rod with symmetric mass distribution.

$$\begin{aligned} m_0 = 0, \quad m_1 = 1[\text{Kg}], \quad m_2 = 0.3[\text{Kg}], \quad c = 0.5[\text{Kg/s}], \\ l_1 = 0.3[\text{m}], \quad l_2 = 0.1[\text{m}], \quad d = 0.05[\text{m}] \quad (13) \\ b_i = l_i/2, \quad J_i = m_i l_i^2 / 12 \quad \text{for } i = 1, 2 \end{aligned}$$

In figure 2 we show numerical time solutions for both dissipative and non-dissipative models. For the non-dissipative model, we use the same formulation and parameters as the dissipative, while taking $c = 0$. In contrast to the nonphysical unbounded behavior of the non-dissipative model, the dissipative model has a bounded oscillatory steady-state behavior.

Next, we demonstrate direction reversal by changing the geometry and mass distribution of the model. We modify the parameters presented in (13) by changing the length of link 2 to $l_2 = 0.2[\text{m}]$ and adding a point-mass m_0 at $b_0 = 0.05[\text{m}]$.

In figure 3 we show how changing the mass distribution of the vehicle influences its movement direction. Without the point-mass, the vehicle moves backward, toward link 1.

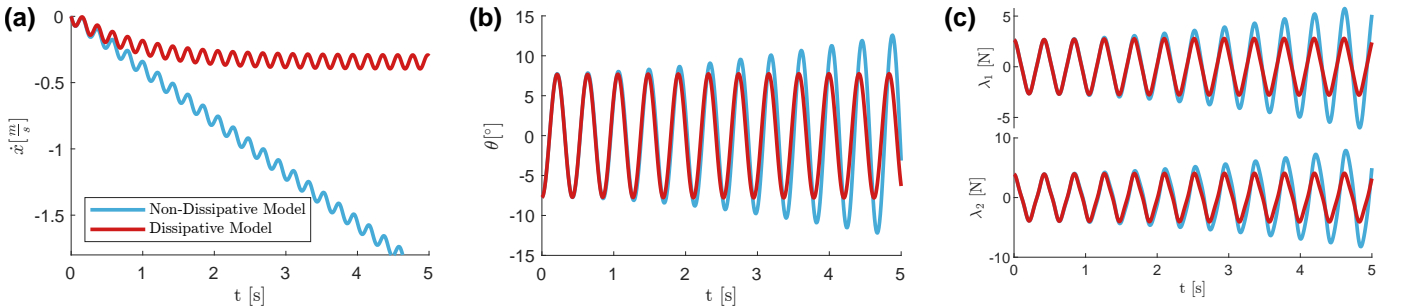


Fig. 2. Numeric simulation results for the dissipative and non-dissipative models, using the parameters in (12), (13). (a) The vehicle's speed in the world frame. (b) The angle of Link 1 about the average direction of progression. (c) Nonholonomic no-skid constraint forces.

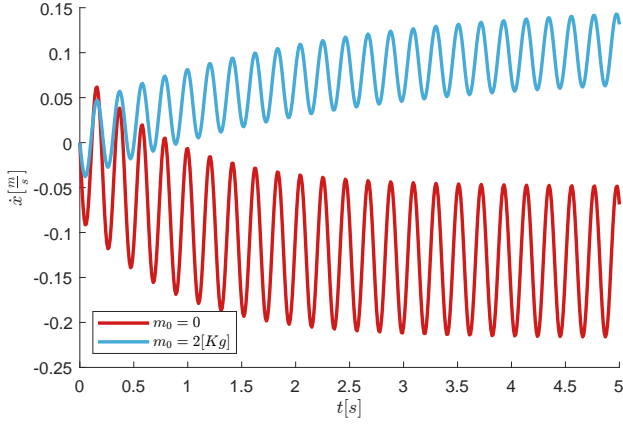


Fig. 3. Direction reversal demonstration using numeric simulation with the parameters in (12), (13), achieved by adding a point-mass to the vehicle.

By adding a point-mass m_0 , the vehicle's speed changes from negative to positive, meaning the vehicle moves forward toward link 2. Using this result, we design an experimental setup that captures the direction reversal phenomenon, as shown below in Section V-C.

IV. ASYMPTOTIC ANALYSIS

In this section, we conduct an approximated asymptotic analysis of the model's dynamics. To conduct the analysis, we first reduce the number of variables by enforcing the constraints. Then, we obtain an asymptotic approximation using perturbation analysis [21].

We define a body-frame velocity vector:

$$\mathbf{v}_b = [v_{\parallel} \quad v_{\perp} \quad \dot{\theta} \quad \dot{\phi}]^T \quad (14)$$

Where v_{\parallel} and v_{\perp} are the velocity components of point P_1 along \mathbf{e}'_1 and \mathbf{e}'_2 directions, i.e. parallel and perpendicular to the vehicle's body.

In (15) we present the transformation from the body-frame velocities to the generalized velocities of the problem.

$$\dot{\mathbf{q}} = \mathbf{R}_b \mathbf{v}_b, \quad \mathbf{R}_b = \begin{bmatrix} \cos \theta & -\sin \theta & 0 & 0 \\ \sin \theta & -\cos \theta & 0 & 0 \\ 0 & 0 & 1 & 0 \\ 0 & 0 & 0 & 1 \end{bmatrix} \quad (15)$$

Next, we use the nonholonomic no-skid constraints in (3) to reduce the dimensionality of the vehicle's dynamics. In (16) we rewrite the constraints in terms of the body-frame velocities.

$$\begin{aligned} \mathbf{W}\dot{\mathbf{q}} &= (\mathbf{W}\mathbf{R}_b) (\mathbf{R}_b^{-1}\dot{\mathbf{q}}) = \mathbf{W}_b \mathbf{v}_b \\ &= \begin{bmatrix} 0 & 1 & 0 & 0 \\ -\sin \phi & \cos \phi & l_1 \cos \phi + l_2 & l_2 \end{bmatrix} \begin{bmatrix} v_{\parallel} \\ v_{\perp} \\ \dot{\theta} \\ \dot{\phi} \end{bmatrix} = \mathbf{0} \end{aligned} \quad (16)$$

This defines two relations between the body-frame velocities. The first directly dictates that the lateral velocity is zero. We use the second row of (16) in order to eliminate $\dot{\theta}$, and

express the equations of motion using a reduced vector of unconstrained velocities, defined as:

$$\mathbf{v}_r = [v_{\parallel} \quad \dot{\phi}]^T \quad (17)$$

We rewrite (16) as a relation between the reduced velocities and the body-frame velocities in (18).

$$\mathbf{v}_b = \mathbf{S}_r \mathbf{v}_r, \quad \mathbf{S}_r = \begin{bmatrix} 1 & 0 \\ 0 & 0 \\ \frac{\sin \phi}{l_2 + l_1 \cos \phi} & -\frac{l_2}{l_2 + l_1 \cos \phi} \\ 0 & 1 \end{bmatrix} \quad (18)$$

We substitute (18) into (15) and obtain a relation between the generalized velocity and the reduced velocity vectors:

$$\dot{\mathbf{q}} = \mathbf{S} \mathbf{v}_b, \quad \mathbf{S} = \mathbf{R}_b \mathbf{S}_r \quad (19)$$

Applying this relation in (8) leads to (20) below. We emphasize that this reduction naturally enforces the nonholonomic no-skid constraints in (16), nullifying all terms involving \mathbf{W} .

$$\mathbf{M}_r(\phi) \dot{\mathbf{v}}_r + \mathbf{B}_r(\phi, \mathbf{v}_r) + \mathbf{D}_r(\phi, \mathbf{v}_r) = \mathbf{F}_r \quad (20)$$

Where:

$$\begin{aligned} \mathbf{M}_r(\phi) &= \mathbf{S}^T \mathbf{M} \mathbf{S} \in \mathbb{R}^{2 \times 2}, \quad \mathbf{F}_r = [0 \quad \tau]^T, \\ \mathbf{B}_r(\phi, \mathbf{v}_r) &= \mathbf{S}^T \mathbf{M} \dot{\mathbf{S}} \mathbf{v}_b + \mathbf{S}^T \mathbf{B} \in \mathbb{R}^{2 \times 1} \end{aligned}$$

The first equation in (20) is decoupled from the second one, and has the structure:

$$\dot{v} = f(v, \phi, \dot{\phi}, \ddot{\phi}) \quad (21)$$

Note that from (21) on, we refer to the forward speed of the vehicle v_{\parallel} as v . We use (21) to solve for v .

To reduce the number of parameters in the problem, we merge the point-mass with link 1. We denote the previous parameters of link 1 with *, so that their modified values are:

$$m_1 = m_1^* + m_0, \quad J_1 = J_1^* + m_0 (b_0 - b_1)^2 \quad (22)$$

Now we nondimensionalize the problem by defining the nondimensional parameters:

$$\alpha = \frac{l_2}{l_1}, \sigma = \frac{d}{l_1}, \kappa = \frac{m_2}{m_1}, \beta_i = \frac{b_i}{l_i}, \eta_i = \frac{J_i}{m_i l_i^2} \quad i = 1, 2 \quad (23)$$

We define the characteristic time of the problem as $t_c = m_1/c$, and denote $\tilde{t} = t/t_c$ and $\tilde{\omega} = \omega t_c$. The nondimensional time-dependent variables are:

$$\tilde{v} = v \frac{t_c}{l_1}, \quad \tilde{v}' = \frac{d\tilde{v}}{d\tilde{t}} = \dot{v} \frac{t_c^2}{l_1}, \quad \phi' = \dot{\phi} t_c, \quad \phi'' = \ddot{\phi} t_c^2 \quad (24)$$

From now on, we analyze the nondimensional problem and drop the tildes for brevity.

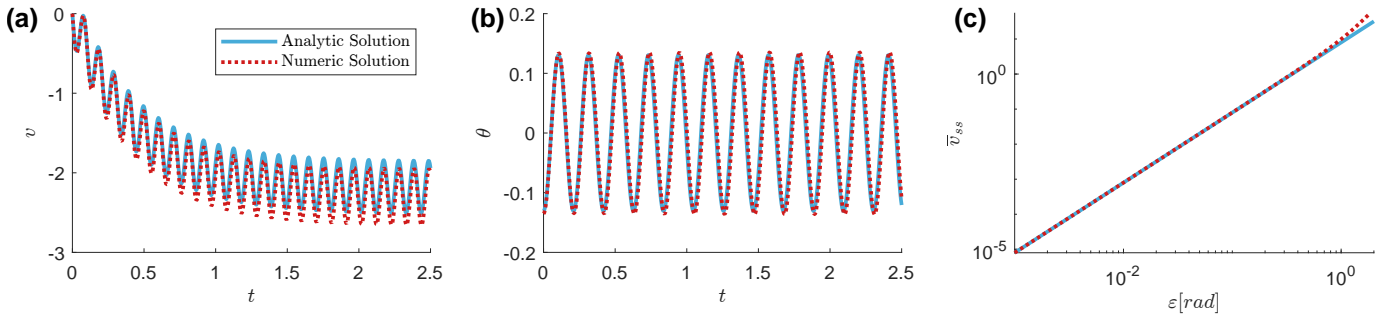


Fig. 4. Comparison between numeric simulation and the leading-order analytic approximation, using the parameters in (12), (13). (a) Time plot of the vehicle's forward speed $v(t)$. (b) Time plot of the orientation angle. (c) Log-log plot of the mean velocity in steady-state vs. the input amplitude.

A. Symmetric input

We first consider the problem under a symmetric time-periodic input of the steering angle, meaning that the input angle defined in (12) has a mean value $\phi_0 = 0$. We write (21) in a nondimensional form:

$$v'(t) = \tilde{f}(v(t), \varepsilon \cos(\omega t), -\varepsilon \omega \sin(\omega t), -\varepsilon \omega^2 \cos(\omega t)) \quad (25)$$

We use perturbation analysis assuming small angle amplitude $\varepsilon \ll 1$, and expand $v(t)$ as a power series in ε :

$$v(t) = v_0(t) + \varepsilon v_1(t) + \varepsilon^2 v_2(t) + \dots \quad (26)$$

We also expand \tilde{f} as a power series in ε . Under zero initial conditions, the leading and first-order solutions are nullified $v_0(t) = v_1(t) \equiv 0$, and $v(t)$ is an even power series. The second-order ODE is in the form of:

$$v_2'(t) = a_1 + a_2 v_2(t) + a_3 \sin(2\omega t) + a_4 \cos(2\omega t) \quad (27)$$

Where a_1, a_2, a_3 appear in Appendix A. We solve (27) and obtain:

$$v_2(t) = b_1 + b_2 e^{-\frac{3t}{1+\kappa}} + b_3 \sin(2\omega t) + b_4 \cos(2\omega t) \quad (28)$$

Where:

$$b_1 = \alpha \omega^2 (\alpha \kappa ((\beta_2 - 2) \beta_2 + \eta_2) + \kappa (\alpha + \beta_2 - 1) + \alpha \beta_1 - \beta_1^2 - \eta_1) / (6(\alpha + 1)^2)$$

b_2, b_3, b_4 appear in Appendix A.

In figure 4(a), we present the nondimensional analytic solution for the forward speed $v(t)$ overlaid with the numeric solution, both obtained with the parameter values as in (13). We check the fit quality between the two solutions in figure 4(c), plotting the mean forward speed in steady-state for different input amplitudes on a log-log scale. The analytic solution is a linear line with a slope of 2 due to its leading order ε^2 , and we see a good alignment between this line and the numeric solution for $\varepsilon \ll 1$ and even for input amplitudes which are closer to 1.

Next, we examine the conditions for direction reversal. We note that the sign of the mean value of the solution in steady-state, b_1 , dictates the direction of movement of the vehicle. In (29) we show ξ , the condition for direction reversal under the assumption $\beta_2 = 1/2$. ξ is positively proportional to b_1 , consisting of the terms that dictate the sign of a_1 . When $\xi > 0$,

the mean velocity of the vehicle is positive, and when $\xi < 0$, the mean velocity of the vehicle is negative.

$$\xi = 4\beta_1 (\alpha - \beta_1) - 4\eta_1 - \kappa (2 - \alpha) + 4\alpha\eta_2\kappa \quad (29)$$

We compare our results to the non-dissipative model in [22], in which the direction reversal condition is determined by the mean acceleration of the vehicle. Under the same assumption of $\beta_2 = 1/2$, we get the same condition for direction reversal.

Using the relation in (18), we can restore the orientation angle of the body. First, we retrieve the orientation's angular velocity:

$$\theta'(t) = \frac{\sin(\phi(t))}{\alpha + \cos(\phi(t))} v(t) - \frac{\alpha}{\alpha + \cos(\phi(t))} \phi'(t) \quad (30)$$

Then, we substitute the velocity's leading-term solution and the steering angle into (30), and integrate with respect to time. We nullify the integration constant so that the steering angle oscillates around zero, and obtain:

$$\theta(t) = -\left(\frac{\alpha}{1+\alpha} \cos(t\omega)\right) \varepsilon + \mathcal{O}(\varepsilon^3) \quad (31)$$

In figure 4(b), we present the nondimensional leading-order orientation angle of the vehicle overlaid with the numeric solution, showing the match between the two.

B. Asymmetric input

We consider an input with small deviation $\phi_0 \ll 1$ from the symmetric case. We write (21) in a nondimensional form and expand $v(t)$ as in (25). As a result, we get the following solution:

$$v(t) = \varepsilon^2 v_2(t) + \varepsilon \phi_0 v_{10}(t) + \mathcal{O}(\phi_0^2 \varepsilon, \phi_0 \varepsilon^2, \varepsilon^3) \quad (32)$$

Where $v_2(t)$ is the second-order approximation, identical to the symmetric case $\phi_0 = 0$ we showed in (28), and $v_{10}(t)$ is a correction term given by:

$$v_{10}(t) = c_2 \left(\sin(\omega t) - e^{-\frac{3t}{1+\kappa}} \right) + c_3 \cos(\omega t) \quad (33)$$

Where the expressions for c_2, c_3 appear in Appendix A.

The correction term in (33) oscillates around zero at steady-state, meaning it does not affect the direction reversal condition. In addition, it oscillates at the input frequency, in contrast to $v_2(t)$ which oscillates at twice this frequency. In figure 5(a), we show a comparison between the numeric simulation and

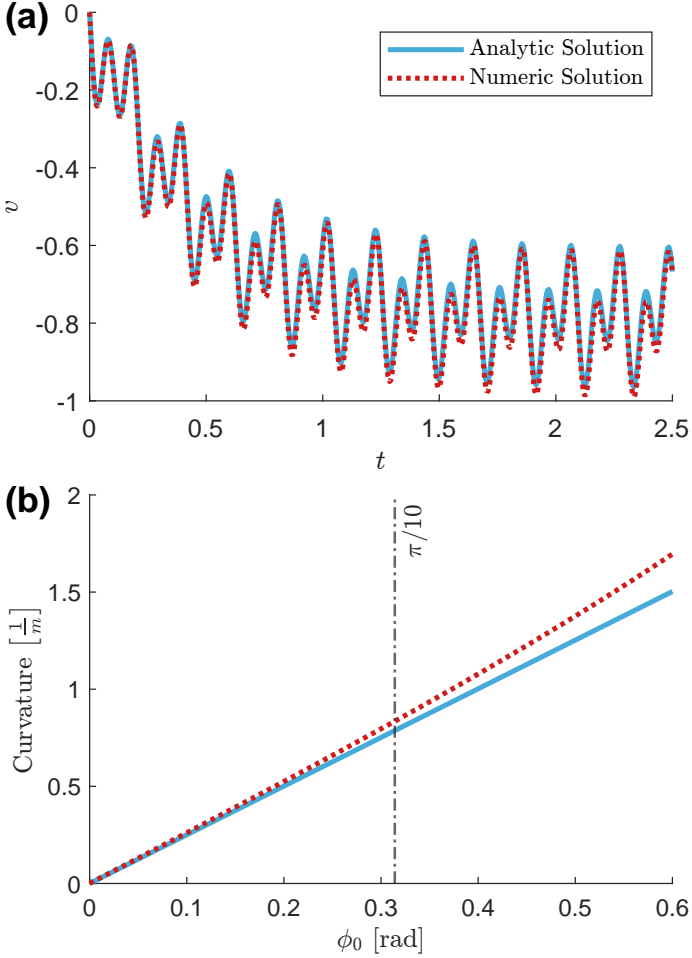


Fig. 5. Comparison between numeric simulation and analytic approximation using (13) and $\varepsilon = \pi/10$. (a) Nondimensional forward speed comparison with $\phi_0 = 5^\circ$. (b) Dimensional mean curvature of the robot’s path, the dash-dotted line is the value of the input angle’s amplitude.

analytic approximation of the forward speed $v(t)$ using the parameters in (13), while incorporating an asymmetric mean input angle.

We use (30) to find the orientation angle’s angular velocity, substituting the velocity as in (32) and expanding as a power series in ε . We show the steady-state solution of the angular velocity in (34). This solution contains a mean value that appears due to the asymmetric input. This constant change in the mean orientation angle of the vehicle leads to a motion along a mean circular arc.

$$\theta'_{ss}(t) = \varepsilon d_0 \sin(\omega t) + \varepsilon^2 \phi_0 (d_1 + d_2 \sin(2\omega t) + d_3 \cos(2\omega t)) + \mathcal{O}(\phi_0^2 \varepsilon) \quad (34)$$

Where expressions for d_0, d_1, d_2, d_3 appear in Appendix A.

In figure 5(b), we present the curvature of the robot’s mean path, depending on the mean input angle. Assuming that the input angle’s mean value is up to the order of its amplitude, we get that the approximated curvature is:

$$\rho = \frac{\overline{\theta'_{ss}}}{\bar{v}} = \frac{\varepsilon^2 \phi_0 d_1 + \mathcal{O}(\phi_0^2 \varepsilon)}{\varepsilon^2 b_1 + \mathcal{O}(\phi_0^2 \varepsilon, \phi_0 \varepsilon^2, \varepsilon^3)} = \frac{d_1}{b_1} \phi_0 + \dots \quad (35)$$

The simulation results show that the curvature is linearly proportional to the mean angle value for an input angle’s mean value smaller than its amplitude. For a larger mean value, (35) is no longer satisfied having a nonlinear relation.

V. EXPERIMENTS

We designed a robot with a modular reconfigurable geometric structure and mass distribution, as shown in figure 6(a). We used a goBILDA kit for the chassis, a servo motor for the relative angle actuation, and an Arduino microcontroller for controlling the servo’s movement.

The experiments were conducted using three main robot configurations, as we show in table I. Those values were taken from the robot’s CAD model. The ‘Nominal Robot’ is the first and basic version of the robot, which was used for the parameter fitting experiments. Then, we modified the robot’s geometry so that a direction reversal would be possible by adding a block mass m_0 onto link 1. In the ‘Backward Configuration’, we extended the length of link 2 so that the forward speed of the vehicle is still negative but close to zero. The ‘Forward Configuration’ is the same configuration while adding the mass block, incorporating the block mass and moment of inertia into the properties of link 1.

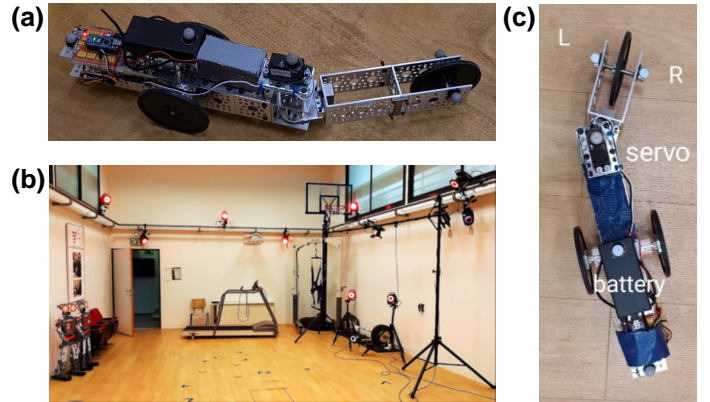


Fig. 6. The robot and experimental setup. (a) The robot in the ‘Forward Configuration’, with the mass block positioned on link 1. (b) VICON camera setup, camera locations are marked with red dots. (c) The four tracking markers, positioned on the robot.

TABLE I
PHYSICAL VALUES FOR DIFFERENT ROBOT’S CONFIGURATIONS

	m_1 [Kg]	m_2 [Kg]	l_1 [m]	l_2 [m]	b_1 [m]	b_2 [m]	J_1 [Kg · m ²]	J_2 [Kg · m ²]
Nominal Robot	0.836	0.29	0.144	0.112	0.0206	0.068	0.0636	0.003873
Backward Configuration	0.836	0.383	0.144	0.208	0.0206	0.098	0.0636	0.01938
Forward Configuration	1.8	0.383	0.144	0.208	0.0426	0.098	0.07757	0.01938

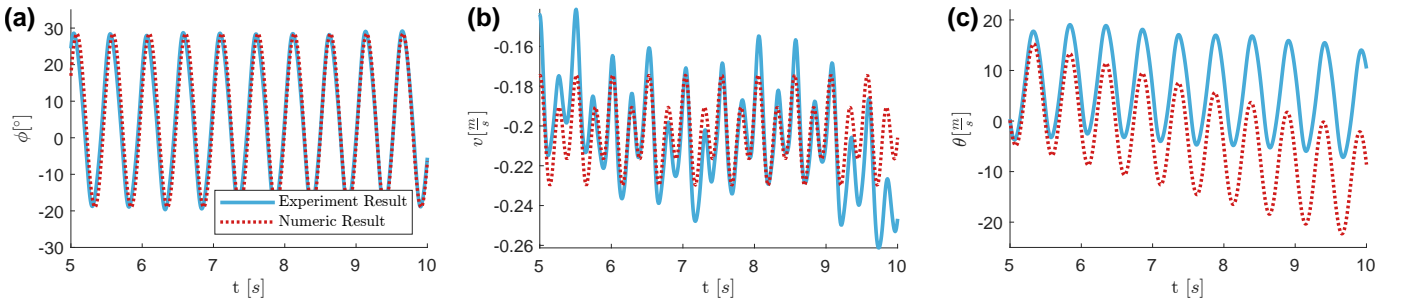


Fig. 7. Comparison between experimental results and simulation results with fitted viscous dissipation coefficient of $c = 0.234 [Kg/s]$. (a) Relative angle between the two links. (b) Vehicle's body-frame velocity. (c) Orientation angle.

A. The experimental setup

We performed motion tracking using the VICON measurement system, using a sampling rate of 120 Hz. This system is equipped with several cameras capable of tracking the location of reflective markers. Both camera setup and the position of the marker on the robot are presented in figures 6(b)-(c). We use Python code to filter the results and calculate the coordinates and velocity of the robot.

B. Parameter fitting

To determine the value of the unknown viscous dissipation coefficient, we conduct a parameter fitting. In this section, all experiments were conducted using the 'Nominal Robot' configuration, as presented in table I, under open-loop input.

First, we look at a specific experiment with an input frequency of 14 radians per second and amplitude of $\pi/6$ radians, shown in figure 7. From figure 7(a), we see that the tracked relative angle is different from the expected input angle by its mean value, amplitude, and frequency. We define the tracked relative angle parameters in (36).

$$\Phi(t) = \Phi_{\text{Mean}} + \Phi_{\text{Amp}} \cos(\Omega t) \quad (36)$$

In this experiment, we find the tracked input angle's parameters: $\Phi_{\text{Mean}} = 4.75^\circ$, $\Phi_{\text{Amp}} = 23.75^\circ$ and $\Omega = 12.36 [rad/s]$, obtained by using the results' extremum points. We conduct a numerical simulation for the tracked input, while hand-tuning the viscous dissipation coefficient. We add to figure 7 the simulation results with the best-fitted coefficient of $c = 0.234 [Kg/s]$. We see that using this model, we were able to capture the behavior of the robot's velocity to a great extent, but were not able to match the actual drift rate of the orientation angle.

We note that in figure 7 we take a specific time window. Outside of this time window, the vehicle does not reach a steady-state and behaves unexpectedly. This behavior can be explained by an outside effect that the robot is sensitive to, and we did not account for while performing the experiment. In the following analysis, we look at each experiment and try to identify a steady-state, such as in figure 7(b), which we can analyze and compare to simulations.

Next, after determining a suitable viscous dissipation coefficient c for a specific experiment, we evaluate its applicability across a variety of experiments with varying input frequencies.

We performed approximately 20 experiments with an input amplitude of 30 degrees and varying input frequencies between 6 and 15 rad/s.

For each experiment, we measure the actual steering angle $\phi(t)$, shown in figure 8(b), which deviates significantly from the commanded input values. We use the actual steering angles as the simulations' input, and use the results to compare with the experiments. In figure 8(a), we show the mean displacement per cycle of each experiment. By hand-tuning the viscous dissipation coefficient, we achieve the best alignment between the experiments and simulations with a value of $c = 0.4 [Kg/s]$.

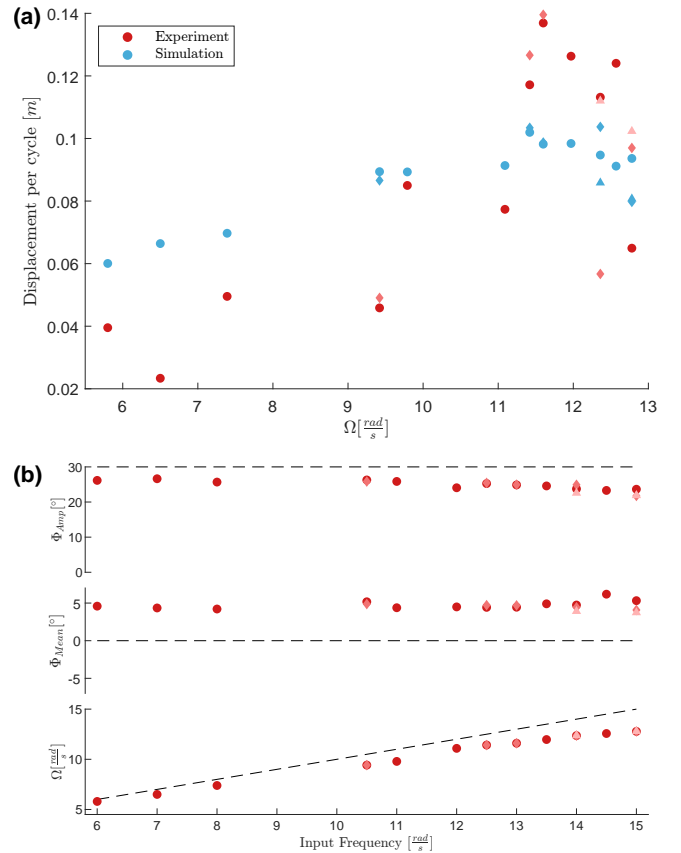


Fig. 8. Dissipation coefficients estimation using frequency-dependent results. (a) Displacement per cycle of different input frequency experiments overlaid with simulation results using $c = 0.4 [Kg/s]$. (b) Captured steering angle properties for different experiments, in dashed line we plot the expected steering angle properties.

From the comparison, we notice that no damping coefficient value matches the results at both high and low input frequencies. In addition, experiments conducted at high frequencies exhibit significant variance between different experiments under the same input. These results highlight the sensitivity of the robot, as previously discussed, and complicate the process of reliable parameter fitting.

C. Direction reversal experiment

Next, we obtain a direction reversal of the robot's movement by placing a mass block on it. In figure 9, we present the experiment results as captured using the tracking system¹. Figure 9(a) contains the robot's forward speed versus time, while figure 9(b) contains snapshots of the robot appearing at fixed time intervals of 6 seconds.

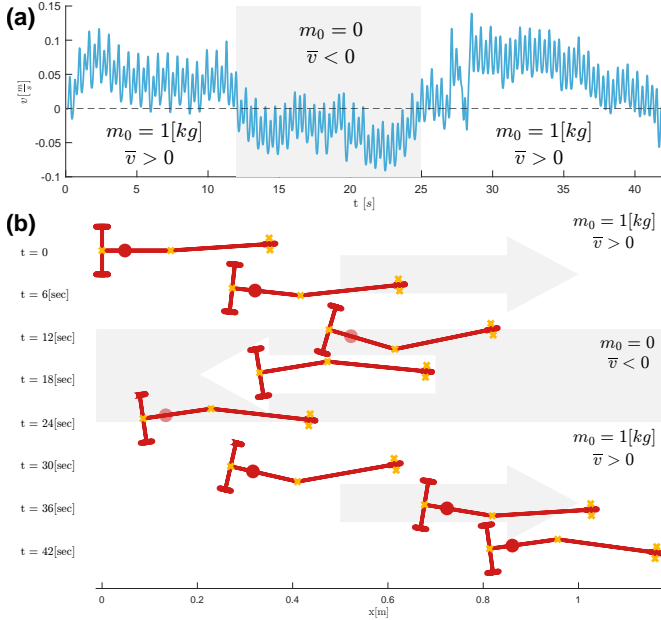


Fig. 9. Direction reversal experiment results, white background - the robot is in 'Forward Configuration', gray background - the robot is in 'Backward Configuration'. (a) Robot speed $v(t)$ measurements. (b) snapshots appearing at fixed time intervals of 6 seconds.

¹This paper has supplementary downloadable material available at https://drive.google.com/file/d/1BL6pWKHyYNvPq4p_D62BVZR0ibrW55cn/view?usp=sharing, provided by the authors. This includes a theoretical and experimental overview of the direction reversal phenomenon. This material is 67.6 MB in size.

The robot starts in the 'Forward Configuration', including the mass block. In the gray sections, we show the time intervals in which the robot is in the 'Backward Configuration', when we take the block off.

From the results, we see that direction reversal is possible by changing the mass distribution of the robot. Note that the human interaction with the robot at the beginning, the ending, and the transition phases between configurations has some effect on the results. Nevertheless, we see a clear difference between forward and backward movement while changing the configuration.

VI. DISCUSSION OF ADDITIONAL EFFECTS

From the comparison results in figure 7(c) and figure 8(a), we see that the model does not capture the behavior of the experimental robot in full. We try to explain the differences by demonstrating the effect of two phenomena on the robot's behavior. The first is the wheels' skidding, and the second is the effect of a slope on the model, which we investigate its impact on the model's behavior.

A. Wheels' skidding

In figure 10(a,c) we show the results of the same experiment as in figure 7, but now we also show the skid velocity $v_{\perp}(t)$ of the rear wheels in figure 7(b). The skid velocity of the vehicle is smaller by one order of magnitude than the forward speed, meaning it is small but not completely negligible.

To simulate this unconstrained model, we remove the non-holonomic no-skid constraints and incorporate a skid dissipation in the same way we incorporate rolling dissipation. We rewrite the skid velocity in terms of the Jacobian:

$$\mathbf{v}_{\perp,i} = \mathbb{J}_{\perp,i}(\mathbf{q})\dot{\mathbf{q}} \quad (37)$$

Using the Jacobian forms in (4) and (37), we write the Rayleigh's dissipation function, when c is the viscous dissipation coefficient at the roll direction of each wheel and c_{\perp} is the viscous dissipation coefficient at the skid direction.

$$\begin{aligned} \mathcal{R}(\mathbf{q}, \dot{\mathbf{q}}) &= \frac{c_{\parallel}}{2} \sum_{i=1}^3 (\mathbf{v}_{\parallel,i})^T (\mathbf{v}_{\parallel,i}) + \frac{c_{\perp}}{2} \sum_{i=1}^3 (\mathbf{v}_{\perp,i})^T (\mathbf{v}_{\perp,i}) \\ &= \frac{1}{2} \dot{\mathbf{q}}^T \left(c_{\parallel} \sum_{i=1}^3 \mathbb{J}_i(\mathbf{q})^T \mathbb{J}_i(\mathbf{q}) + c_{\perp} \sum_{i=1}^3 \mathbb{J}_{\perp,i}(\mathbf{q})^T \mathbb{J}_{\perp,i}(\mathbf{q}) \right) \dot{\mathbf{q}} \end{aligned} \quad (38)$$

We use the Euler-Lagrange method as in (7), while nullifying the constraints.

$$\mathbf{M}(\mathbf{q})\ddot{\mathbf{q}} + \mathbf{B}(\mathbf{q}, \dot{\mathbf{q}}) + \mathbf{D}(\mathbf{q}, \dot{\mathbf{q}}) = \mathbf{F}_q \quad (39)$$

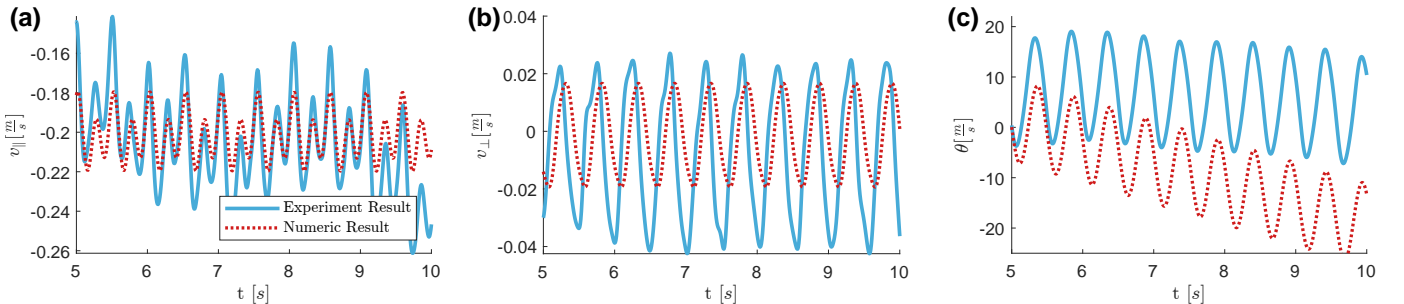


Fig. 10. Comparison between experimental results and simulation results with fitted viscous dissipation coefficients of $c_{\parallel} = 0.095[Kg/s]$, $c_{\perp} = 4[Kg/s]$. (a) Vehicle's body-frame rolling velocity. (b) Vehicle's body-frame skid velocity. (c) Orientation angle.

Where $\mathbf{M}(\mathbf{q})$ and $\mathbf{B}(\mathbf{q}, \dot{\mathbf{q}})$ are derived the same way as in (8) and:

$$\mathbf{D}(\mathbf{q}, \dot{\mathbf{q}}) = \frac{\partial \mathcal{R}}{\partial \dot{\mathbf{q}}} \quad (40)$$

To conduct the simulation, we divide the matrices into passive and active coordinates the same way as in Section III, and rearrange into matrix form when the unknown vector consists of the passive coordinates' acceleration and the input torque.

$$\begin{bmatrix} \mathbf{M}_{pp} & \mathbf{0}^{3 \times 1} \\ \mathbf{M}_{pa}^T & -1 \end{bmatrix} \begin{bmatrix} \ddot{\mathbf{q}}_p \\ \tau \end{bmatrix} = - \begin{bmatrix} \mathbf{M}_{pa} \ddot{\mathbf{q}}_a + \mathbf{B}_p + \mathbf{D}_p \\ \mathbf{M}_{aa} \ddot{\mathbf{q}}_a + \mathbf{B}_a + \mathbf{D}_a \end{bmatrix} \quad (41)$$

We hand-tune the viscous dissipation coefficients, and then choose the best-fitted coefficients $c_{\parallel} = 0.095[Kg/s]$ and $c_{\perp} = 4[Kg/s]$. The rolling dissipation coefficient obtained in this section is much smaller than the one that was obtained using the constrained model. This difference may explain the difference between the simulation and the experiments.

B. Uphill Slope

While experimenting, we noticed that experiments with the same input frequencies behave differently, as shown in figure 8(a). We check if the inconsistencies of the levelness of the ground's surface on which the experiment was conducted have a significant influence on the results.

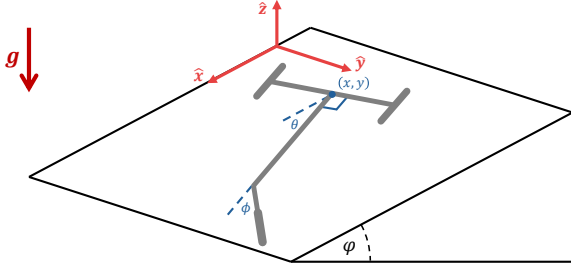


Fig. 11. Gravitational-planar model of the Twistcar.

We model this as an uphill slope of angle φ , as we show in figure 11. We take the same constrained-dissipative planar model we showed in figure 1(a), and incorporate potential energy into it. For this section, we take $m_0 = 0$ and the Potential energy is defined as:

$$V = \mathbf{g} \cdot (m_1 \mathbf{r}_{c1} + m_2 \mathbf{r}_{c2}), \quad \mathbf{g} = g \begin{bmatrix} -\sin \varphi & 0 \end{bmatrix}$$

We add to (8) the gravitational term \mathbf{G} :

$$\begin{aligned} \mathbf{M}(\mathbf{q})\ddot{\mathbf{q}} + \mathbf{B}(\mathbf{q}, \dot{\mathbf{q}}) + \mathbf{D}(\mathbf{q}, \dot{\mathbf{q}}) + \mathbf{G}(\mathbf{q}) &= \mathbf{F}_q + \mathbf{W}^T(\mathbf{q})\Lambda \\ \mathbf{W}(\mathbf{q})\ddot{\mathbf{q}} + \dot{\mathbf{W}}(\mathbf{q})\dot{\mathbf{q}} &= 0 \end{aligned} \quad (42)$$

Where $\mathbf{M}(\mathbf{q})$, $\mathbf{B}(\mathbf{q}, \dot{\mathbf{q}})$ and $\mathbf{D}(\mathbf{q}, \dot{\mathbf{q}})$ are identical to the matrices used in (8), and:

$$\mathbf{G} = \frac{\partial V}{\partial \mathbf{q}} = \begin{bmatrix} -g(m_1 + m_2) \sin \varphi \\ 0 \\ g \sin \varphi [(b_1 m_1 + l_1 m_2) \sin \theta + b_2 m_2 \sin (\theta + \phi)] \\ g b_2 m_2 \sin (\theta + \phi) \sin \varphi \end{bmatrix}$$

We simulate the gravitational model with the 'Nominal Robot' configuration from table I, and a symmetric input with

$\Phi_{\text{Amp}} = 23.75^\circ$ and $\Omega = 12.36[\text{rad/s}]$. We conduct the simulation three times. The first simulation is with a slope angle of $\varphi = 0$, which is equivalent to the model we used so far. In comparison, we conduct two more simulations with slope angles of $\varphi = 0.5^\circ$, shown in red, and $\varphi = 1^\circ$, shown in yellow.

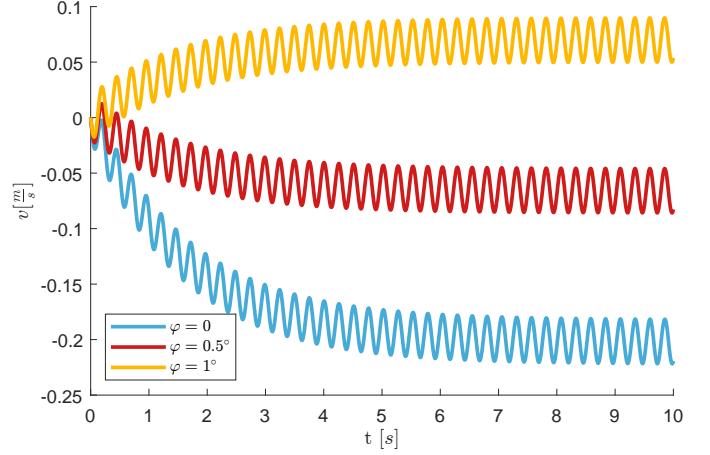


Fig. 12. Comparison between uphill slope simulations with different slopes, for the 'Nominal Robot' configuration.

In figure 12 we demonstrate how significantly the levelness of the ground's surface influences the robot's speed, capable of changing the movement direction of the vehicle for a slope angle as small as 1° . This result may explain the significant variance observed in figure 8 between experiments conducted under the same input, as the ground conditions were not a primary focus during the experiments.

VII. CONCLUSIONS

In this work, we used theoretical analysis in order to investigate the dynamic behavior of the dissipative Twistcar and compared it to experiments. Both theoretical work and experiments showed that in the dissipative Twistcar, a direction reversal is obtainable by changing its geometry and mass distribution.

The analysis involved perturbation expansion and was validated using numeric simulations. Using the analysis, we designed a modular robot demonstrating direction reversal. To determine the unknown viscous dissipation coefficient of the model, we conducted multiple experiments over a wide range of input frequencies, and also ran our simulation with input that was modified to match the actual measurements of joint angle in the experiment. By hand-tuning this coefficient, we found the best-fitting one as measured experimentally.

At the end of the work, we discussed some limitations of the model. First, one of our assumptions is no wheels' skidding. However, experimental results indicate that skidding is present and not negligible. Second, we showed that the levelness of the ground's surface can greatly influence the behavior of the robot.

Some future work includes improving the experimental setup. By utilizing a better controller, it will be possible to obtain a more reliable input angle with a symmetric input.

Such a controller will be able to input a wider range of frequencies, possibly capturing a direction reversal depending on the input's amplitude, as was shown in [19], [22].

Another future approach may involve the dissipation model that was used. The viscous dissipation model is a simple model that does not depend on normal ground reaction forces, for example. Incorporating a more generalized friction model may lead to a better alignment between the experimental and theoretical work.

We also suggest using our approach to analyze other models using perturbation expansion and comparing it to experiments. For example, this can be done to the three-linked snake with one passive joint [4], the rotor-actuated passive-steering Twistcar [31], and other vehicles with passive joints [32].

ACKNOWLEDGMENTS

The authors wish to express their gratitude to Professor Alon Wolf and the BRML team at the Technion for their support and for granting access to their laboratory facilities. In addition, sincere appreciation is extended to Ariel Bar-Yehuda, the lab engineer, for his invaluable help with the experiments. We also express our gratitude to Snir Carmeli and Dolev Freund for their efforts in conducting the experiments.

APPENDIX A

EXPLICIT COEFFICIENTS OF THE APPROXIMATE ANALYTIC SOLUTION

$$\begin{aligned} \Delta_1 &= [6(\alpha + 1)^2]^{-1} \\ \Delta_2 &= (4(\kappa + 1)^2\omega^2 + 9)^{-1} \\ \Delta_3 &= ((\kappa + 1)^2\omega^2 + 9)^{-1} \\ \Delta_4 &= [6(\alpha + 1)^3]^{-1} \end{aligned}$$

$$\begin{aligned} a_1 &= -\alpha\omega^2 [\alpha\beta_1 - \beta_1^2 + \kappa(\alpha + \beta_2 - 1) - \eta_1 + \alpha\kappa(\eta_2 + \beta_2(\beta_2 - 2))] \Delta_1 a_2 \\ a_2 &= -3/(\kappa + 1) \\ a_3 &= \alpha\omega(\sigma^2 + 2\alpha + 2) \Delta_1 a_2/2 \\ a_4 &= \alpha\omega^2 [\alpha\beta_1 + \beta_1^2 + \kappa(\alpha + \beta_2 + 1) + \eta_1 - \alpha\kappa(\eta_2 + \beta_2(\beta_2 - 2))] \Delta_1 a_2 \\ b_2 &= -2\alpha\omega^2 [2\alpha\beta_1(\kappa + 1)^2\omega^2 + \alpha\beta_2^2\kappa(2(\kappa + 1)^2\omega^2 + 9) + (2(\kappa + 1)^2\omega^2 + 9)(\alpha\eta_2\kappa - \eta_1) + 2\beta_2\kappa(-((2\alpha - 1)(\kappa + 1)^2\omega^2) - 9\alpha) \\ &\quad + 3(\alpha\kappa + \alpha + 2(\kappa + 1)\sigma^2 - 2\kappa + 1) + 2(\alpha - 1)\kappa(\kappa + 1)^2\omega^2 - \beta_1^2(2(\kappa + 1)^2\omega^2 + 9)] \Delta_1 \Delta_2 \\ b_3 &= 3\alpha\omega [2(\kappa + 1)\omega^2(\beta_2\kappa(\alpha\beta_2 - 2\alpha - 1) - \alpha\beta_1 + \alpha\eta_2\kappa - \beta_1^2 - \eta_1) - 2(\alpha + 1)\kappa(\kappa + 1)\omega^2 - 3(\alpha + 2\sigma^2 + 1)] \Delta_1 \Delta_2 \\ b_4 &= 3\alpha\omega^2 [3\kappa(\beta_2(\alpha\beta_2 - 2\alpha - 1) + \alpha\eta_2) - 3\alpha\beta_1 - (\alpha + 1)(\kappa - 2) - 3\beta_1^2 - 3\eta_1 + 4(\kappa + 1)\sigma^2] \Delta_1 \Delta_2 \\ c_2 &= 6\alpha\omega^2 (3\alpha\kappa((\beta_2 - 2)\beta_2 + \eta_2) + \alpha\kappa + \alpha - 3\beta_1^2 - 3\eta_1 + 2(\kappa + 1)\sigma^2 - 2\kappa + 1) \Delta_1 \Delta_3 \\ c_3 &= 6\alpha\omega((\kappa + 1)\omega^2(\alpha\kappa((\beta_2 - 2)\beta_2 + \eta_2) - \beta_1^2 - \eta_1) - 3(\alpha + 2\sigma^2 + 1) - \kappa(\kappa + 1)\omega^2) \Delta_1 \Delta_3 \end{aligned}$$

$$\begin{aligned} d_0 &= \alpha\omega/(\alpha + 1) \\ d_1 &= \alpha\omega^2 [\alpha\beta_2^2\kappa((\kappa + 1)^2\omega^2 + 18) + \alpha\beta_1((\kappa + 1)^2\omega^2 + 9) + 3(4\alpha\kappa + \alpha + 2(\kappa + 1)\sigma^2 - 5\kappa + 1) + \beta_2\kappa(-((2\alpha - 1)(\kappa + 1)^2\omega^2) - 36\alpha + 9) \\ &\quad + ((\kappa + 1)^2\omega^2 + 18)(\alpha\eta_2\kappa - \eta_1) + (\alpha - 1)\kappa(\kappa + 1)^2\omega^2 - \beta_1^2((\kappa + 1)^2\omega^2 + 18)] \Delta_3 \Delta_4 \\ d_2 &= 3\alpha\omega \left\{ -(\kappa + 1)\omega^2 [2\alpha\beta_1((\kappa + 1)^2\omega^2 + 9) + 2\beta_2\kappa((6\alpha + 1)(\kappa + 1)^2\omega^2 + 27\alpha + 9) - 3\alpha\beta_2^2\kappa(2(\kappa + 1)^2\omega^2 + 9) \right. \\ &\quad \left. + 3(2(\kappa + 1)^2\omega^2 + 9)(\eta_1 - \alpha\eta_2\kappa) + 3\beta_1^2(2(\kappa + 1)^2\omega^2 + 9)] + 3(\kappa + 1)\omega^2(2\alpha(2\kappa + 5) - 10(\kappa + 1)\sigma^2 + \kappa + 10) \right. \\ &\quad \left. + 2(\kappa + 1)^3\omega^4(\alpha(\kappa + 2) - \kappa + 2) + 27(\alpha - 4\sigma^2 + 1) \right\} \Delta_2 \Delta_3 \Delta_4 \\ d_3 &= 9\alpha\omega^2 [\alpha\beta_2^2\kappa(5(\kappa + 1)^2\omega^2 + 18) - \alpha\beta_1((\kappa + 1)^2\omega^2 + 9) - \beta_1^2(5(\kappa + 1)^2\omega^2 + 18) - \beta_2\kappa((10\alpha + 1)(\kappa + 1)^2\omega^2 + 36\alpha + 9) \\ &\quad + (5(\kappa + 1)^2\omega^2 + 18)(\alpha\eta_2\kappa - \eta_1) + (\kappa + 1)^2\omega^2(\alpha(\kappa + 2) + 4(\kappa + 1)\sigma^2 - 3\kappa + 2) + 9(\alpha + 2(\kappa + 1)\sigma^2 - \kappa + 1)] \Delta_2 \Delta_3 \Delta_4 \end{aligned}$$

REFERENCES

- [1] A. M. Bloch, *Basic Concepts in Geometric Mechanics*. New York, NY: Springer New York, 2003, pp. 119–174.
- [2] J. Neimark and N. Fufaev, *Dynamics of Nonholonomic Systems*, ser. Translations of mathematical monographs. Amer. Mathem. Society, 1972.
- [3] J. Ostrowski, A. Lewis, R. Murray, and J. Burdick, “Nonholonomic mechanics and locomotion: the snakeboard example,” in *Proc. of the 1994 IEEE Int. Conf. on Robotics and Automation (ICRA)*, vol. 3, 1994, pp. 2391–2397.
- [4] L. Rizyaev and Y. Or, “Locomotion dynamics of an underactuated three-link robotic vehicle,” 2024, arXiv:2407.21540.
- [5] E. M. Purcell, “Life at low reynolds number,” *American Journal of Physics*, vol. 45, no. 1, pp. 3–11, 1977.
- [6] O. Wiezel and Y. Or, “Optimization and small-amplitude analysis of purcell’s three-link microswimmer model,” *Proc. of the Royal Society A: Mathematical, Physical and Engineering Sciences*, vol. 472, no. 2192, pp. 1471–2946, 2016.
- [7] E. Kanso, J. E. Marsden, C. W. Rowley, and J. B. Melli-Huber, “Locomotion of articulated bodies in a perfect fluid,” *Journal of Nonlinear Science*, vol. 15, no. 4, pp. 255–289, 2005.
- [8] E. Virozub, O. Wiezel, A. Wolf, and Y. Or, “Planar multi-link swimmers: Experiments and theoretical investigation using “perfect fluid” model,” *Robotica*, vol. 37, no. 8, p. 1289–1301, 2019.
- [9] R. L. Hatton and H. Choset, “Geometric swimming at low and high reynolds numbers,” *IEEE Transactions on Robotics*, vol. 29, no. 3, pp. 615–624, 2013.
- [10] B. Buchanan, T. Dear, S. Kelly, M. Travers, and H. Choset, “The geometric structure of externally actuated planar locomoting systems in ambient media,” 2021, arXiv:2108.06442.
- [11] J. Ostrowski, J. Burdick, A. Lewis, and R. Murray, “The mechanics of undulatory locomotion: the mixed kinematic and dynamic case,” in *Proc. of 1995 IEEE Int. Conf. on Robotics and Automation*, vol. 2, 1995, pp. 1945–1951.
- [12] E. A. Shammass, H. Choset, and A. A. Rizzi, “Geometric motion planning analysis for two classes of underactuated mechanical systems,” *The Int. Journal of Robotics Research*, vol. 26, no. 10, pp. 1043–1073, 2007.
- [13] —, “Towards a unified approach to motion planning for dynamic underactuated mechanical systems with non-holonomic constraints,” *The Int. Journal of Robotics Research*, vol. 26, no. 10, pp. 1075–1124, 2007.
- [14] S. Stanchenko, “Non-holonomic Chaplygin systems,” *Journal of Applied Mathematics and Mechanics*, vol. 53, no. 1, pp. 11–17, 1989.
- [15] S. David Kelly, M. J. Fairchild, P. M. Hassing, and P. Tallapragada, “Proportional heading control for planar navigation: The Chaplygin beanie and fishlike robotic swimming,” in *2012 American Control Conf. (ACC)*, 2012, pp. 4885–4890.
- [16] J. Osborne and D. Zenkov, “Steering the Chaplygin sleigh by a moving mass,” in *Proc. of the 44th IEEE Conf. on Decision and Control*, 2005, pp. 1114–1118.
- [17] P. S. Krishnaprasad and D. P. Tsakiris, “Oscillations, se(2)-snakes and motion control: A study of the roller racer,” *Dynamical Systems*, vol. 16, no. 4, pp. 347–397, 2001.
- [18] T. Dear, S. D. Kelly, M. Travers, and H. Choset, “Mechanics and control of a terrestrial vehicle exploiting a nonholonomic constraint for fishlike locomotion,” in *Dynamic Systems and Control Conf.*, vol. 2, 2013.
- [19] S. Bazzi, E. Shammass, D. Asmar, and M. T. Mason, “Motion analysis of two-link nonholonomic swimmers,” *Nonlinear Dynamics*, vol. 89, no. 4, pp. 2739–2751, 2017.
- [20] O. Chakon and Y. Or, “Analysis of Underactuated Dynamic Locomotion Systems Using Perturbation Expansion: The Twistcar Toy Example,” *Journal of Nonlinear Science*, vol. 27, no. 4, pp. 1215–1234, 2017.
- [21] A. Nayfeh, *Perturbation Methods*. London: Wiley, 2008.
- [22] O. Halvani and Y. Or, “Nonholonomic dynamics of the Twistcar vehicle: asymptotic analysis and hybrid dynamics of frictional skidding,” *Nonlinear Dynamics*, vol. 107, no. 4, pp. 3443–3459, 2022.
- [23] I. A. Bizyaev, A. V. Borisov, and I. S. Mamaev, “Exotic Dynamics of Nonholonomic Roller Racer with Periodic Control,” *Regular and Chaotic Dynamics*, vol. 23, no. 7, pp. 983–994, 2018.
- [24] Kilin Alexander A., Ivanova Tatiana B., Karavaev Yury L., and Yefremov Kirill S., “Theoretical and experimental investigations of the controlled motion of a roller racer,” *Theoretical and Applied Mechanics*, 2025.
- [25] V. Fedonyuk and P. Tallapragada, “Stick–slip motion of the chaplygin sleigh with a piecewise-smooth nonholonomic constraint,” *Journal of Computational and Nonlinear Dynamics*, vol. 12, no. 3, p. 031021, 2017.
- [26] T. Yona and Y. Or, “The wheeled three-link snake model: singularities in nonholonomic constraints and stick–slip hybrid dynamics induced by Coulomb friction,” *Nonlinear Dynamics*, vol. 95, no. 3, pp. 2307–2324, 2019.
- [27] N. Sidek and N. Sarkar, “Dynamic modeling and control of nonholonomic mobile robot with lateral slip,” in *3rd Int. Conf. on Systems (ICONS)*, 2008, pp. 35–40.
- [28] S. Bazzi, E. Shammass, and D. Asmar, “A novel method for modeling skidding for systems with nonholonomic constraints,” *Nonlinear Dynamics*, vol. 76, no. 2, pp. 1517–1528, 2014.
- [29] T. Dear, S. D. Kelly, M. Travers, and H. Choset, “Snakeboard motion planning with viscous friction and skidding,” in *2015 IEEE Int. Conf. on Robotics and Automation (ICRA)*, 2015, pp. 670–675.
- [30] R. M. Murray, Z. Li, and S. S. Sastry, *A Mathematical Introduction to Robotic Manipulation*. Boca Raton, FL, USA: CRC Press, 1994.
- [31] Z. Yu, J. Paul, and Y. Or, “Nonholonomic dynamics of steer-free rotor-actuated twistcar,” in *3rd Int. Nonlinear Dynamics Conf. (NODYCON)*, 2023.
- [32] C. Rodwell and P. Tallapragada, “Induced and tunable multistability due to nonholonomic constraints,” *Nonlinear Dynamics*, vol. 108, no. 3, pp. 2115–2126, 2022.